A computational study on osmotic chemotaxis of a reactive Janusbot

Shirsendu Mitra, Anshuman Pasupalak, Saptarshi Majumdar, and Dipankar Bandyopadhyay

View Online   Export Citation   CrossMark

ARTICLES YOU MAY BE INTERESTED IN

AIP
Publishing

A computational study on osmotic chemotaxis of a reactive Janusbot

Shirsendu Mitra,[1] (iD) **Anshuman Pasupalak,**[2] **Saptarshi Majumdar,**[2] **and Dipankar Bandyopadhyay**[1,3,a] (iD)

AFFILIATIONS

[1] Department of Chemical Engineering, Indian Institute of Technology Guwahati, Guwahati, Assam 781039, India
[2] Department of Chemical Engineering, Indian Institute of Technology Hyderabad, Hyderabad 502285, Telangana, India
[3] Centre for Nanotechnology, Indian Institute of Technology Guwahati, Guwahati, Assam 781039, India

[a] Author to whom correspondence should be addressed: dipban@iitg.ac.in

ABSTRACT

We explore the chemotaxis of an elliptical double-faced Janus motor (Janusbot) stimulated by a second-order chemical reaction on the surfaces, $aA + bB \rightarrow cC + dD$, inside a microfluidic channel. The self-propulsions are modeled considering the full descriptions of hydrodynamic governing equations coupled with reaction–diffusion equations and fluid–structure interaction. The simulations, employing a finite element framework, uncover that the differential rate kinetics of the reactions on the dissimilar faces of the Janusbot help in building up enough osmotic pressure gradient for the motion as a result of non-uniform spatiotemporal variations in the concentrations of the reactants and products around the particle. The simulations uncover that the mass diffusivities of the reactants and products along with the rates of forward and backward reactions play crucial roles in determining the speed and direction of the propulsions. Importantly, we observe that the motor can move even when there is no difference in the total stoichiometry of the reactants and products, $(a + b) = (c + d)$. In such a scenario, while the reaction triggers the motion, the difference in net-diffusivities of the reactants and products develops adequate osmotic thrust for the propulsion. In contrast, for the situations with $a + b \neq c + d$, the particle can exhibit propulsion even without any difference in net-diffusivities of the reactants and products. The direction and speed of the motion are dependent on difference in mass diffusivities and reaction rate constants at different surfaces.

Published under license by AIP Publishing. https://doi.org/10.1063/5.0025816

I. INTRODUCTION

Self-propulsion of a motor inside a fluid medium[1–7] has been under extensive research attention in the recent past owing to its scientific and translational importance. A number of naturally occurring processes, such as pinocytosis[8,9] or phagocytosis of cells,[10,11] ATP synthesis,[12,13] or diffusion of bio-particles through the cell membrane, are some of the very well-known examples of such motions, driven by the chemical potential gradients. Furthermore, the bacterial locomotion[14,15] and spermatozoa locomotion[16] by the movement of flagella are also some of the very interesting biomimetic prototypes of self-motile systems. Of late, inspired by these examples, a wide variety of micro- and nanoscale self-propelling objects have been artificially synthesized, which undergo propulsion under the influence of electric[14–18] or magnetic field,[19–21] chemical potential,[22,23] acoustic[24,25] or light waves,[26,27] and surface

tension forces,[28–30] among others. These motions are also under intensive scientific exploration in the form of the fundamental studies on the particle migrations involving electrophoresis, magnetophoresis, chemotaxis, chemophoresis, sono-taxis, photo-taxis, or Marangoni motion.

In particular, the chemical stimuli responsive locomotion of the "double-faced" Janus particles,[31,32] namely, the "Janusbot," has gained considerable interest owing to their potential in multifarious separation,[33,34] transport,[37] and biomedical applications.[35] The locomotion driven by a chemical potential gradient is, in general, termed "chemotaxis."[36,37] Furthermore, when a particle moves under a chemical potential gradient, the propulsion is also termed the "chemophoresis."[38,39] The scientists for generations are perhaps attempting to artificially synthesize mesoscale synthetic self-propelling robots, namely, microbots or nanobots, undergoing "chemotaxis" or "chemophoresis," emulating many of the

omnipresent biological processes. For example, artificially synthe-sized nanoscale bimetallic spheres[40,41] or rods[42,43] are found to show "random" chemotactic migrations inside a peroxide bath where the speed or propulsion increases with H_2O_2 concentration in the fuel.[44] On the other hand, a number of previous works show that the tubular microbots and Janus motors can show a "unidirec-tional" motion.[45] In this regard, the stimulus of pH variation in the direction of the motion has also been explored.[46] However, the physics associated with such motions are rather difficult to compre-hend owing to the coupling of the complex multiphase hydrody-namics involving gas–liquid–solid interactions along with the pres-ence of multi-component reaction and diffusion kinetics.[23,47] At the mesoscale, the time and length scales of such processes alongside the speed and direction of motions may largely depend on the reac-tivity or diffusivity of the reactants and products surrounding the motor.[48]

Importantly, a number of previous studies show that the ran-domly moving chemotactic motors can also be remotely guided by the magnetic[49] or electric fields.[50] Such synthetic motors have shown the capacity of loading cargo, essentially a drug, and deliv-ering it to a specific location under a remote guidance.[51–53] How-ever, in most of the natural processes, such directional locomotion occurs under the sole influence of chemical potential gradients.[5,6,54] In particular, amoeba, *Dictyostelium discoideum*, or *Escherichia coli* is found to exploit the uneven distribution of the chemicals to estab-lish the chemical potential gradient and undergo chemotaxis.[55,56] A few recent works show the possibility of similar motions at the synthetic level.[57–60] However, despite the availability of a fairly large amount of literature, the origin of such motions as well as the vari-ations in speed and direction with the various internal and exter-nal conditions are some of the aspects that require more delibera-tions. In particular, the contributions of various kinetic parameters such as rate constants of the reactions and diffusion coefficients of the species require much deeper attention from the scientific perspective.

In view of this background, we focus on the motion of an ellip-tical "double-faced" Janusbot having different kinetics of reactions at the half-surfaces. The use of elliptical shape opens up the pos-sibility of exploring the influence of any sphere-like object using the same framework. The motions of such motors are simulated considering the full descriptions of two-dimensional (2D) hydrody-namic governing equations coupled with reaction–diffusion trans-port equations and fluid–structure interaction before enforcing the appropriate boundary conditions. In the simulations, the particle acquires motion by converting the chemical energy into the mechan-ical one. We consider a second-order reaction with the stoichiom-etry $aA + bB \rightarrow cC + dD$ having different rate constants on the chemically heterogeneous faces of the particle. The use of such a generic reaction opens up the possibility of studying all the other rate kinetics, e.g., zeroth-, first-, or pseudo-first-order reactions, using the same framework under various asymptotic limits. The simula-tions use a finite element framework to uncover that the differential rate kinetics on the surfaces of the Janusbot eventually help in build-ing up an osmotic pressure gradient across the particle. In a way, the spatiotemporal variations in the concentrations of the reactants and products due to the chemical reaction help in manifesting such a pressure gradient to drive the motor. Subsequently, the particle speed is found to depend on various parameters, such as viscosity

and density of fluid, concentrations of reactants and products, rates of reactions at the surfaces, diffusivities of the reactants and prod-ucts, and the size and shape of the motor. The simulated results are found to match closely with the ones available with the experimental reports. The integrated continuum model proposed here delivers the platform for further comprehensive deliberations on the chemotaxis of reactive Janusbots. The present study is perhaps among the first few reports, where the relative contributions of reaction kinetics and component diffusion on chemophoretic migration of a particle have been explored.

II. PROBLEM FORMULATION

A. Governing equations

Figure 1 schematically shows the geometry considered for the simulations of the chemophoretic motion of a particle of elliptical cross section inside a microfluidic channel filled with a liquid. The liquid inside the microfluidic channel contains four different com-ponents, two of which (*A* and *B*) are reactants undergoing chemi-cal reactions to produce the pair of products (*C* and *D*) following the stoichiometry $aA + bB \rightarrow cC + dD$. In the theoretical formu-lation, a mixed coordinate system is employed in order to model the problem. For the analytical model proposed later, a polar coor-dinate system (r, θ) with the origin at the center of the particle, $r = 0$, has been employed, as shown in Fig. 1. The transport equations for the fluid flow inside the rectangular microchannel are numeri-cally solved with the help of a 2D Cartesian coordinate system (x, y). The fluid inside the channel is considered to be Newtonian and incompressible.

In this problem formulation, the bold variables indicate vec-tors, the bold variables with double overbars indicate tensors, partial derivative of a variable is denoted by the symbol ∂, the notation ∇ is the gradient operator, the letter "I" denotes the identity tensor, and the superscript "T" stands for the transpose of a matrix. The com-ponents of a vector are symbolized as $\mathbf{u}[u, v]$ and $\mathbf{u}_s[u_s, v_s]$, which denote the fluid velocity and displacement vector of the solid par-ticle, respectively. The concentration of the *i*th species is shown by
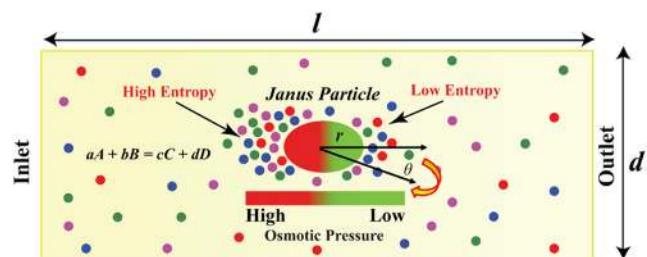

FIG. 1. Schematically shows the chemophoretic movement of an elliptical particle inside a liquid filled microchannel as a result of local osmotic pressure imbalance, which is generated as a result of nonuniform distribution of solute components around the particle. An asymmetric catalytic chemical reaction is taking place on the particle surface with different reaction kinetics at the two different halves of the particle. There are two reactants, which give two products following the reaction stoichiometry $aA + bB \rightarrow cC + dD$.

c_i. The symbols t, ρ, ρ_s, μ, and D_i represent time, density of fluid, density of the solid particle, viscosity of the electrolyte, and diffusivity of the ith species, respectively. The letter "M" represents the molar concentration, i.e., mol/m^3. The concentration of the ith species (c_{ri}) of the reactant has been governed by the following scalar transport equation:

$$\partial c_{ri}/\partial t + u_i \cdot \nabla c_{ri} = D_{ri}\nabla^2 c_{ri} - k \prod c_{ri}. \qquad (1)$$

Here, i signifies reactants, A and B. The term $\prod c_{ri}$ represents the multiplication of all the reactants. The concentration of the products is also governed by the following scalar transport equation:

$$\partial c_{pi}/\partial t + u_i \cdot \nabla c_{pi} = D_{pi}\nabla^2 c_{pi} + k \prod c_{ri}. \qquad (2)$$

In Eq. (2), c_{pi} denotes the concentration of different products, C and D. The last term in Eqs. (1) and (2) appears for the reaction near the particle surface, which couples Eqs. (1) and (2). For the fluid flow, the following continuity equation along with Navier–Stokes equations is solved:

$$\nabla \cdot \mathbf{u} = 0, \qquad (3)$$

$$\rho \frac{D\mathbf{u}}{Dt} = -\nabla p + \mu(\nabla^2 \mathbf{u}) - \nabla \pi. \qquad (4)$$

The last term in Eq. (4) is the force due to the osmotic pressure imbalance ($\nabla \pi$), which originates due to the generation of products C and D after the reaction of A and B, following different rate kinetics at the dissimilar faces of the Janus particle. Importantly, there is no external pressure gradient imposed in the system, which ensures that the flow is solely due to the osmotic pressure imbalance. The osmotic pressure (π) is calculated from the following equation:

$$\pi = RT \sum c_i. \qquad (5)$$

Here, the osmotic pressure being a colligative property is expressed as a function of the summation of concentrations of all the components, $\sum c_i$. Thus, in a way, the set of Eqs. (1)–(5) are coupled with each other.

The fluid–structure interaction (FSI) has been considered to track the motion of the particle. The equations associated with the FSI are as follows:

$$\rho_s(\partial^2 \mathbf{u}_s/\partial t^2) - \nabla \cdot \overline{\overline{\sigma}} = 0, \qquad (6)$$

$$\overline{\overline{\sigma}} = -p\overline{\overline{I}} + \mu(\nabla \mathbf{u} + \nabla \mathbf{u}^T). \qquad (7)$$

Here, the symbols ρ_s and $\overline{\overline{\sigma}}$ represent the density of the solid and the stress tensor of a Newtonian fluid, respectively. All the symbols used in this article are enlisted in Table I. From Eq. (7), it is clear that the fluid flow stress imparts a force to drive the particle, and the same is the basis of the present study. It is further assumed that the osmotic pressure imbalance is rather small, and the particle (e.g., a silica ball) is rigid and non-deformable during the movement. Furthermore, the rotational chemophoretic movements are not considered, which may be present in the particles with asymmetric shape. This aspect has been avoided owing to the complexity associated with the remeshing of the surrounding assymetric particles under such circumstances.

TABLE I. The symbols and values or range of values of the parameters used.

Symbol	Variable/notation	Unit	Value
c_{ri}	Concentration of the ith reactant	M/m^3	. . .
c_{pi}	Concentration of the ith product	M/m^3	. . .
D_{ri}	Diffusivity of the ith reactant	m^2/s	1–5×10^{-9}
D_{pi}	Diffusivity of the ith product	m^2/s	1–5×10^{-9}
D_r	Average diffusivity of all the reactants	m^2/s	. . .
D_p	Average diffusivity of all the products	m^2/s	. . .
K_L	Reaction rate constant in the left half of the particle	M^{-1} s^{-1}	0.88–8.8
K_R	Reaction rate constant in the right half of the particle	M^{-1} s^{-1}	0.88–8.8
A, B	Symbolize two reactants	. . .	. . .
a, b	Stoichiometric coefficients of reactants A and B	. . .	1
C, D	Symbolize two products	. . .	. . .
c, d	Stoichiometric coefficients of products C and D	. . .	1
ρ	Density of liquid	kg/m^3	1000
μ	Viscosity of liquid	Pa s	0.0023
ρ_s	Density of the solid particle	kg/m^3	2200
d_c	Width of the channel	μm	250
l_c	Length of the channel	μm	500
a_p	Length of the semi-major axis of the elliptical particle	μm	10
b_p	Length of the semi-minor axis of the elliptical particle	μm	7
l	Distance measured from the particle surface	μm	. . .
u_p	Particle velocity	μm/s	. . .
π	Osmotic pressure	Pa	. . .
R	Universal gas constant	J/(kg K)	8.314
T	Absolute temperature	K	298

B. Boundary conditions

For Eqs. (1) and (2), Dirichlet boundary conditions at the inlet and outlet of the channel are enforced. At the inlet, $x = 0$, $c_{ri} = c_{ri0}$ is enforced for the reactant while initially the concentration of the product (c_{pi}) is kept zero at both the ends of the channel. At the outlet $x = l$, normal flux boundary conditions $-\mathbf{n} \cdot \nabla D_i c_{ri} = 0$ for the reactants (c_{ri}) are enforced. For the auto-chemophoretic motion, the constant concentration (c_{ri}) in the beginning of the simulation ($t = 0$) without no inflow and no flux at any of the ends of the channel are deployed. The continuity and Navier–Stokes equations (3) and (4) have been solved by taking the no slip and impermeability boundary conditions ($u = v = 0$ at $y = 0$, d) at the walls of the microchannel. To ensure that the motion of the particle along with the fluid inside the channel occurs due to the chemical gradient only, both the ends of the channel are kept at atmospheric pressure to ensure a non-existing pressure gradient across the channel. For FSI, the two-way coupling is enforced between the fluid and the

particle. For this purpose, the continuity of velocity conditions, $\mathbf{u} = \dot{\mathbf{u}}_s$, has been enforced on the particle surface, while a no-slip condition is enforced along the inner wall of the tube. Zero displacement ($\mathbf{u}_s = 0$) and zero speed ($\dot{\mathbf{u}}_s = 0$) of the particle at initial time ($t = 0$) have been enforced to meet the two boundary conditions necessary to solve Eq. (6). The hydrodynamic stress is evaluated from the coupled momentum equations.

III. NUMERICAL METHODOLOGY

A finite element method (FEM) based commercial CFD simulation software, COMSOL Multiphysics$^{\text{TM}}$, is used for discretization and the solution of the coupled set of equations (1)–(7) with the aforementioned boundary conditions. COMSOL Multiphysics is chosen for the present work as this is a robust simulation package. This software also has efficient multiphysics coupling and moving deforming mesh options, which are the prime requirements of the current work. For the grid-independence study, we have taken four different mesh sizes and compared the line averaged values of component concentrations (c_{r1} and c_{p1}), and also the particle speed for a particular set of parameters, as depicted in Table II.

It is evident from Table II that ~40 000 elements could give a grid-independent solution.

The software uses the Galerkin least-squares (GLS) method along with the second order elements for speed calculations and first-order elements to discretize the equations. The velocity and pressure profile calculations are done using the segregated predictor–corrector method with incremental pressure correction. Consistent initialization and time-marching are taken care of by the software using a second-order backward difference method with a suitable time step size of ~10^{-4} s.

IV. VALIDATION

A. Analytical model

A simple analytical model has been developed to validate the results obtained from CFD simulations. For this purpose, the particle is assumed to be spherical in shape, and hence, a three-dimensional spherical (r, θ, and φ) coordinate system is taken. It is assumed that all the derivatives with respect to polar coordinates are zero. Hence, the radial direction in space and time coordinate survives for the purpose of all the calculations of this part. A set of unsteady reaction–diffusion equations has been considered for the reactant and product. Moreover, for this validation, a first-order

elementary reaction following the stoichiometry $R \rightarrow S$ is used. The reaction kinetics of the stated reaction follows the rate equation, $-dC_R/dt = dC_P/dt = kC_R$. The values of the reaction rate constants are varied with the position to incorporate differential rates at two different ends of the particle. The reaction and diffusion equations, which determine the concentration profiles as a function of space and time for both reactant and product, are

$$\partial c_R/\partial t = D_R \nabla^2 c_R - k c_R, \tag{8}$$

$$\partial c_P/\partial t = D_P \nabla^2 c_P + k c_R. \tag{9}$$

In order to solve Eqs. (8) and (9), boundary conditions that describe the underlying phenomenon are set. The one-dimensional solution space, which is assumed for the analytical study, is $[R, R + l_a]$, where l_a is the active distance measured from the particle surface ($r = R$) after which the effect of reaction–diffusion is not that much effective. The boundary conditions pertinent to the reactant are

$$c_R(R, t) = c_{RS}, \ c_R(r, 0) = c_{RS}, \ \nabla c_R(l_a, 0) = 0, \tag{10}$$

and for the product, the boundary conditions are

$$c_P(R, t) = c_{PS}, \ c_P(r, 0) = c_{RS}, \ \nabla c_R(l_a, 0) = 0. \tag{11}$$

Here, c_{RS} and c_{PS} are steady concentrations of the reactant and product on the particle surface and also everywhere at the initial time ($t = 0$).

The concentration profiles obtained from the simulations and analytical model are compared and contrasted to ensure the accuracy of the proposed numerical CFD code. It may be noted here that the use of FSI and deforming mesh in the simulations affects the species concentration profiles around the particle with time. Furthermore, the derivation of analytical solutions employing moving reference frames is more than cumbersome and perhaps beyond the scope of the present study. Thus, we elucidate a simple static reference frame for the semi-analytical calculations of the concentration profile surrounding the motor to validate the simulated results. The differential equations (8) and (9) with the help of the boundary conditions [Eqs. (10) and (11)] are solved numerically using commercial package MATHEMATICA$^{\text{TM}}$ to evaluate the concentration profiles around the sphere. Different kinetic parameters based on differential reaction rate kinetics at two different sides of the particle are employed. Figures 2(a) and 2(b) show the comparison of profiles at the left and right halves of the Janus particle, where the first-order reaction rate constants are $k_R = 8.5$ s^{-1} and $k_L = 1.7$ s^{-1}. These figures show a good match between numerical and semi-analytical profiles near the particle surface, and they deviate away from the surface. The deviations can be attributed to the asymptotic nature of the semi-analytical model in the absence of FSI, deforming mesh, non-linear terms, and coupled advection–reaction–diffusion hydrodynamics, among many other reasons. The asymptotic match obtained from this study establishes the authenticity of further calculations using these sets of equations and numerical methodologies involved in COMSOL Multiphysics.

Another validation attempt has been made to justify the accuracy of the simulations wherein we compare the particle speed with the speed of Stokes's migration, as reported in Ref. 23. The average particle speed for Stokes migration is calculated from the following

TABLE II. The grid-independence study details.

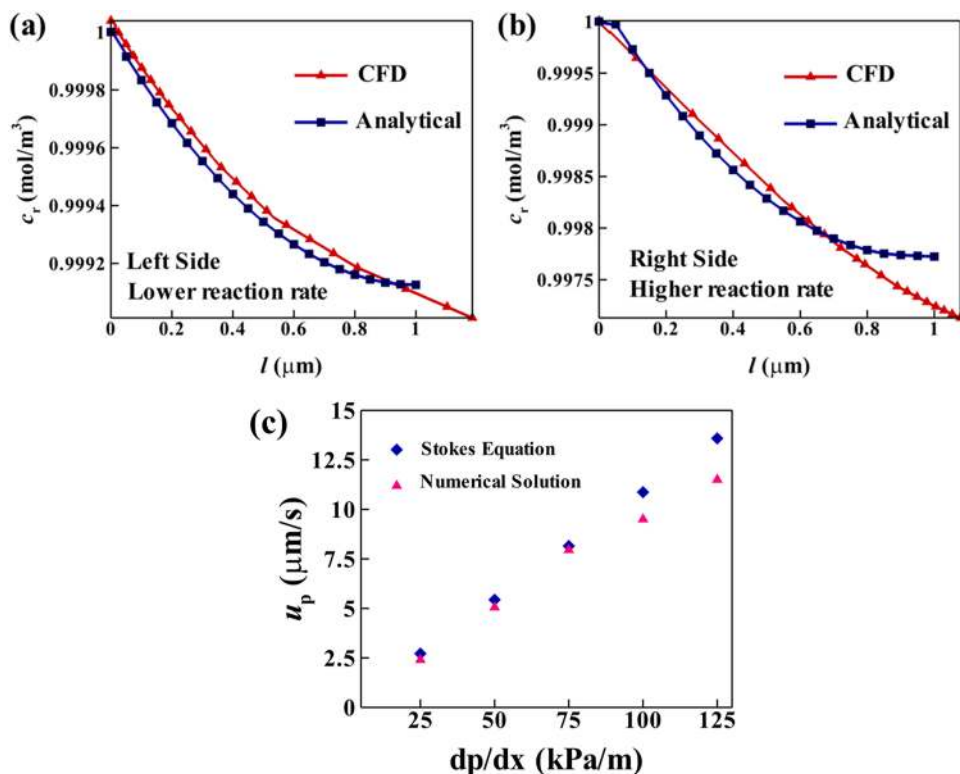| No.	No of elements	Line averaged c_{r1}	Line average c_{p1}	Particle speed (μm/s)
Mesh 1	25 000	0.995	0.0008	4.2
Mesh 2	35 000	0.985	0.0011	4.72
Mesh 3	40 000	0.983	0.0013	4.80
Mesh 4	50 000	0.982	0.0014	4.82

FIG. 2. (a) Shows the comparison of the concentration profile of the reactant, at the left-hand side of the Janus particle, obtained from CFD numerical simulation and analytical solution. (b) shows a similar comparison for the right-hand side of the Janus particle. A first-order reaction has rate constants k_L = 1.75 and k_R = 8.9 s^{-1} in the left and right halves of the Janus particle, respectively. The diffusivity of the reactant (D_r) is kept constant as 3×10^{-9} m^2/s. (c) shows the particle speed comparison between numerical results and analytical calculation by Stokes's speed equation.

equation: $u_p = (|\Delta p/\Delta x|)L_s^2/4\mu$.[23] Here, L_s and $|\Delta p/\Delta x|$ represent the characteristic Stokes length (length from the particle surface up to which gradient exists) and the magnitude of the pressure gradient, respectively. We have done an analysis where the pressure gradient from the numerical simulation is evaluated before replacing the same in the aforementioned Stokes expression. For this study, L_s and μ are taken as 1 μm and 0.0023 Pa s, whereas the $|\Delta p/\Delta x|$ values are varied from 25 kPa to 125 kPa/m with an interval of 25 kPa/m. Figure 2(c) shows the comparison between the analytical and numerical speeds. The plot discloses a close match with a slight deviation at higher pressure gradients. In the analytical solution, the viscous drag force is neglected, which can be the reason behind such conditional discrepancy. However, despite such marginal deviation, good match is observed, which corroborates the accuracy of the numerical schemes employed.

V. RESULTS AND DISCUSSION

In the present study, we consider two types of chemotactic motions of a Janusbot, (i) auto-chemophoresis—the motor moves because of the local osmotic pressure gradient and (ii) guided-chemophoresis—the particle is moving inside a microchannel with an existing concentration gradient of the reactants along with local chemical reactions in the proximity of the particle. For the guided-chemophoretic case, we study the motion of a Janusbot ($d_p \sim 1$ μm), which moves in a confined microchannel of diameter 5 μm and

length 15 μm. Furthermore, the auto-chemophoretic motion of a Janusbot ($d_p \sim 5$ μm) has been studied in a relatively wider microchannel of diameter 250 μm and length 500 μm owing to the sole influence of the local osmotic pressure gradient. Videos 1 and Video 2 in the supplementary material show the typical chemophoresis and auto-chemophoresis of a Janus particle simulated in this work, respectively.

A. Auto-chemophoresis

The chemically heterogeneous faces of the Janusbot facilitate second order catalytic chemical reactions at different rates with the reactants, *A* and *B*, present in the surrounding fluid to produce *C* and *D* at a different rate in the close proximity of the particle. The distributions of the reactants and products generate a net osmotic force to propel the particles inside the channel. A set of simulations have been performed with particles of different shapes, such as elliptical, circular, rectangular, or square, keeping all other simulation parameters unchanged. The particle geometries are considered in such a manner that they have equal perimeters of ~56 μm in order to ensure the same available "area" for the reaction. The initial concentrations of reactants are taken as 1 mol/m^3, while the products are assumed to be absent at time t = 0. The rate constant of the reaction is varied from ~0.88 M^{-1} s^{-1} to 8.8 M^{-1} s^{-1}. The model also assumes that the left-hand side of the particle offers higher reaction kinetics (k_L = 8.8 M^{-1} s^{-1}) compared to the right side (k_R = 0.88 M^{-1} s^{-1}). In such a scenario, the higher diffusivity for the products

$(D_p = 4 \times 10^{-9}$ m^2/s) compared to the diffusivity of reactants $(D_r = 2 \times 10^{-9}$ m^2/s) drives the particle in the positive x-direction—the left side to the right side.

Figure 3(a) shows the profile of $\Delta\pi$ for all the particles simulated. The plots suggest that the shapes of the Janusbots have a significant influence on the osmotic pressure distribution around the particle. Figure 3(b) shows that the particle speed increases with $\Delta\pi$, with an exception for circular and elliptical particles. The plot suggests that although the oblate-elliptical particle generates a relatively lower osmotic pressure drop across the surface, a lower drag force due to the streamlining of the geometry toward the flow helps them in attaining the maximum speed. Eventually, the particle Reynolds number for all remains far less than 1, which ensures that the Stokes drag,[61] a function of shape, plays an important role in deciding the average particle speed. The simulations uncover that the vertical ellipse shows a maximum $\Delta\pi$, whereas the square shaped motor shows the minimum $\Delta\pi$. However, the speed of both the particles is nearly the same. On the other hand, the vertical ellipse shows a more drag friction than that of the square one. In view of this result, we decide to explore the results with oblate-elliptical geometries. The choice of elliptical geometry is also attributed to the facts that (i) the shape can be asymptotically reduced to any circular geometry by tuning the lengths of major and minor axes; (ii) the experimental micro-/nanobots can never be an exactly circular or spherical; and (iii) the streamlined elliptical geometry helps in reducing the friction during the motion, which leads to a faster migration inside a fluidic medium.

It may be noted here that for the auto-chemophoretic movement of the motor, a particle with a 10 μm semi-major axis and a 7 μm semi-minor axis is considered. The entire channel is filled with the solution having an equal concentration (1 mol/m^3) of reactants (A and B), which are expected to decompose on the chemically heterogeneous surface of the motor at different rates of the catalytic reaction to generate the products. Subsequently, the combined influences of differential catalytic surface activities of the Janusbot and net mass diffusivity (of the reactants and products) around the particle will generate the required osmotic pressure gradient ($\Delta\pi$) for the self-propulsion. Video 1 in the supplementary material shows the

auto-chemophoretic movement inside a channel. The supplementary material further describes about Video 1. Thus, for the proposed system, there are two different time scales. The reaction time scale is of the order of $c_0{}^n/k$, while the diffusion time scale is $t = l^2/D$. Here, c_0 and n signify the initial concentration of a component present in the system and the order of the reaction, respectively. The magnitudes of the parameters considered for the simulations ensure that the diffusion time scale (~ms) is much higher than the reaction time scale (~μs).

Figure 4 shows the development of the average concentration profiles with time due to the reaction and subsequent development of the osmotic pressure around the particle. Figures 4(a) and 4(c) show the profiles for the left-hand side of the particle, whereas Figs. 4(b) and 4(d) show the profiles for the right-hand side of the particle. Here, the left-hand side of the Janusbot has a higher reaction rate ($k_L = 8.8$ M^{-1} s^{-1}) as compared to the right-side ($k_R = 0.88$ M^{-1} s^{-1}). Thus, with time, the left-face consumes more reactants to yield more products compared to the right-face. The concentration of the reactants (products) reaches up to 0.975 mol/m^3 (0.012 mol/m^3) on the left-side, whereas it goes up to 0.984 mol/m^3 (0.007 mol/m^3) on the right-side after 0.5 s. Figures 4(c) and 4(d) show the decrease in the absolute value of the average osmotic pressure with time at the left- and right-hand sides of the particle.

Figure 5 shows two different Janusbots, one has a higher reaction rate on the right-face ($k_R = 8.8$ M^{-1} s^{-1}), as shown in Fig. 5(a), while the other on the left-face ($k_L = 8.8$ M^{-1} s^{-1}), as shown in Fig. 5(d). Importantly, the diffusivity of the products ($D_p = 3 \times 10^{-9}$ m^2/s) is also kept higher as compared to the same of the reactants ($D_r = 1.5 \times 10^{-9}$ m^2/s). Thus, for the Janusbot shown in Fig. 5(a), a higher reaction rate at the right-face gives rise to a lower concentration of the reactant in the right-hand side and a higher concentration of the product in the left-hand side of the particle, as shown in Figs. 5(b) and 5(c), respectively. Distribution of these components around the particle makes an inhomogeneous scenario to create a $\Delta\pi$ across the particle, as shown in Fig. 5(a). The higher osmotic pressure developed at the right half of the particle facilitates a motion toward the left side. Figure 5(d) shows a particle having
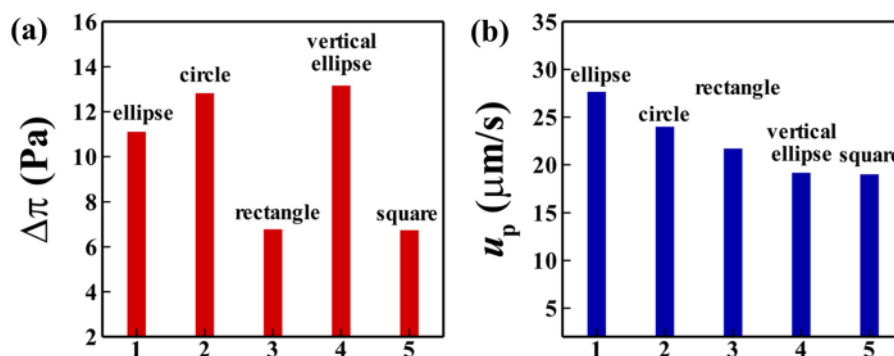

FIG. 3. Auto-chemophoretic motions of Janusbots with different shapes inside a channel of diameter (d) 250 μm and length (l_c) 500 μm. The 2D projections of the particles look like ellipse, circle, rectangle, vertical ellipse, and square. Inside the microchannel, the liquid is filled, which contains reactants A and B that undergo the reaction at the particle surface. For all the cases, the perimeter of the particle is kept 56 μm. (a) shows the average osmotic pressure difference ($\Delta\pi$), which is obtained by taking the average along with a line extended up to 10 μm both sides from the particle surface. (b) compares and contrasts the speed of the particles with different shapes.
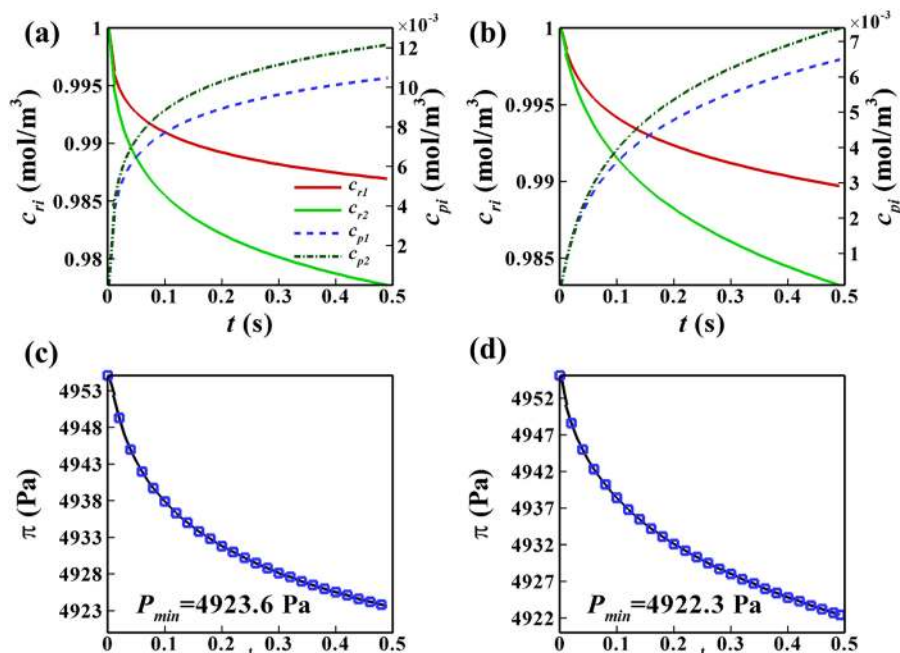
FIG. 4. (a) Shows the average concentration vs time (t) profiles (taken across a line along the axis away from the particle surface) of the reactants (c_{ri}) and products (c_{pi}) at the left-hand side of the particle. (b) shows the same average concentration of reactants (c_{ri}) and products (c_{pi}) at the right-hand side of the particle. (c) and (d) show the average osmotic pressure (π) vs time (t) profile for the left- and right-hand sides of the particle.

similar arrangement; however, the orientation is opposite, i.e., the left half of the particle offers a higher reaction rate constant (k_L). The contour profiles of the reactant and the product are as shown in Figs. 5(e) and 5(f), respectively. These figures suggest the possibility

of the movement from left to right owing to the nature of osmotic pressure buildup.

Figure 6 shows the concentration profiles of the reactants and products alongside the profile of the osmotic pressure along the axis
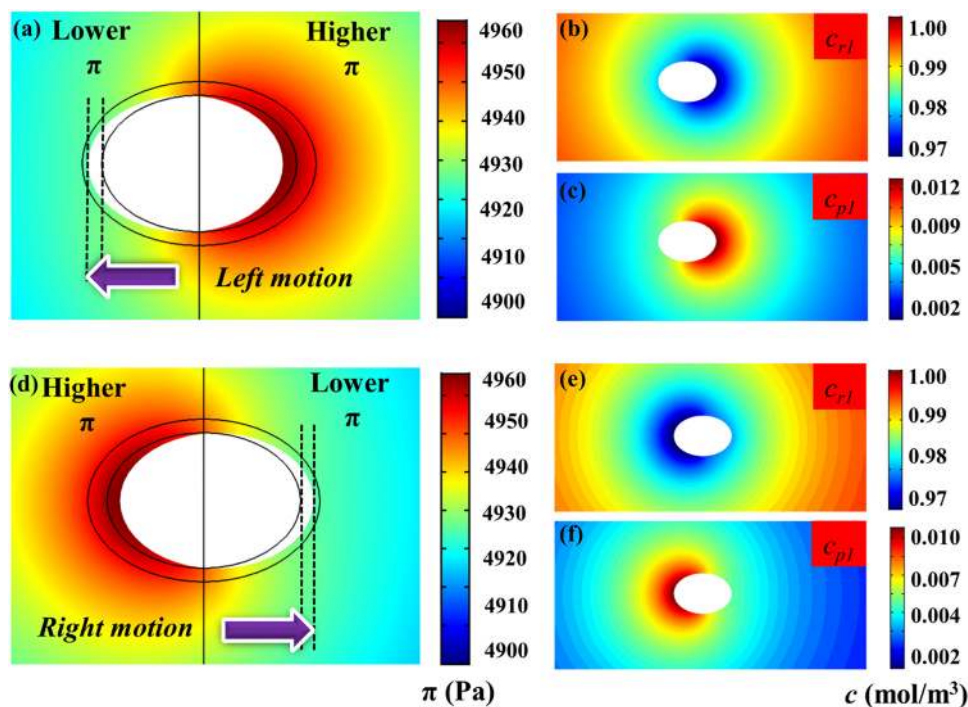

FIG. 5. (a) Shows the near steady contours of space averaged osmotic pressure (π) around the particle showing auto-chemophoretic movement after 0.4 s, surrounding a Janusbot having a higher reaction rate (k_R) at the right-face and undergoing a motion from right to left of the channel. (b) and (c) show the contours of the concentration of a reactant and a product. (d) shows the contour of osmotic pressure, surrounding a particle having a higher reaction rate (k_L) at the left-hand side, with a particle moving left to right. (e) and (f) show the concentration of contours of a reactant and a product surrounding the particle, respectively.
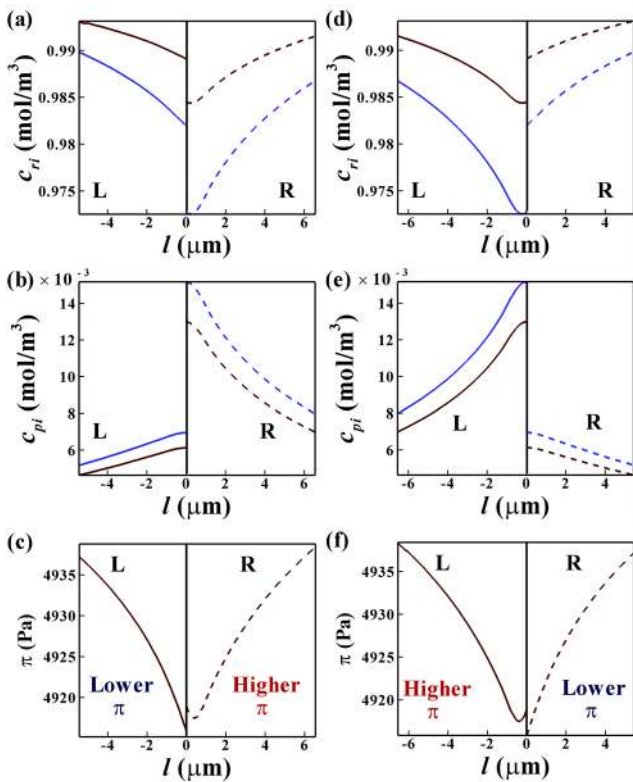
FIG. 6. (a)–(c) Show the near steady state profiles around the particle showing auto-chemophoretic movement (after 0.4 s) of the space averaged reactant/product concentrations and osmotic pressure with the distance from the particle surface (*l*). The plots correspond to the Janus particle having a higher rate constant on the right-side. (d)–(f) show the near steady state contours (after 0.4 s) of the space averaged reactant/product concentrations and osmotic pressure with the distance from the particle surface (*l*), where the rate constant at left-half is higher.

of the channel in the vicinity of the particle surface. The analysis presented in Fig. 6 corresponds to the simulations shown in Fig. 5, after the space averaged profiles reach an approximate steady state ~0.4 s. For the ease of representation, the coordinate of the particle surface is taken as "0" on both the ends of the particle. The distance from the right-hand side of the particle surface is taken as positive (+*l*), while the same from the left-surface is considered as negative (−*l*). Figures 6(a) and 6(b) show that the concentrations of the reactants (products) diminish (increase) near the particle surface, while the same increases (reduce) away from the particle surface. These two plots correspond to the simulation shown previously in Fig. 5(a).

Figure 6(c) shows the average osmotic pressure profiles along a line taken from the particle surface. The plot suggests that a difference of ~1 Pa–5 Pa has been sufficient to move the particle ahead. Figures 6(d) and 6(f) show reactant and product concentration profiles corresponding to the simulation shown in Fig. 5(d). A comparison between Figs. 6(c) and 6(f) highlights the buildup of the osmotic pressures around the particles, whereas in Figs. 5(a) and 5(d), it is exactly opposite, thus leading to the motions from right-to-left

and left-to-right, respectively. The development of the concentration profiles of the components depends mainly on the reaction kinetics. However, the development of $\Delta\pi$ across the particle is also depended on the net diffusivity of the components. The diffusivities of the components help in alleviating the inhomogeneity of concentration of the species across the particle to influence the $\Delta\pi$.

In Fig. 7, we consider some such interesting situations, for example, the diffusivities of the products are taken to be different from those of reactants; however, the diffusivity of the reactants (and products) is kept to be the same. Furthermore, two different orientations of the particle are taken, one having a higher reaction rate constant on the left-hand side and another having a higher rate constant on the right-hand side of the particle. For each situation, two different combinations are considered, (i) higher diffusivities of the reactants and (ii) higher diffusivities of the products.

In Figs. 7(a) and 7(c), the product to reactant diffusivity ratio (D_p/D_r) is kept at 3.5, whereas for Figs. 7(b) and 7(d), D_p/D_r is 4.0. These figures suggest that the buildup of $\Delta\pi$ enhances with the increase in the D_p/D_r. Furthermore, Figs. 7(a) and 7(c) show that when the reactants have higher diffusivities, the osmotic pressure is lower at the particle surface, while it increases away from the particle surface. In comparison, Figs. 7(b) and 7(d) show that when the products have higher diffusivities, the osmotic pressure is higher near the particle surface, while it diminishes with the distance from the particle surface. Interestingly, Figs. 7(a)–7(d) also show that the change in the direction of the motion is possible solely by tuning D_p/D_r, as indicated by the arrows on these figures. This is quite different from the cases discussed in Figs. 5 and 6 where the variation in the rate constant at the faces of the Janusbot was the only reason for the motion as well as change in the direction of the motion.

The simulated results shown in Fig. 7 uncover that when the left face of the Janusbot can degrade the reactants at a higher rate [Fig. 7(a), higher k_L, and low D_p/D_r], a larger concentration of the products near the left face helps in building up a larger osmotic pressure, which facilitates the movement from left to right. In comparison, for such a system, if the D_p/D_r is increased beyond a critical, the products with higher diffusivities go away fast from the left face to ensure that the osmotic pressure is higher at the right side leading to a motion from right to left [Fig. 7(b), higher k_L and high D_p/D_r]. In comparison, when the right face of the Janusbot can degrade the reactants at a higher rate [Fig. 7(c), higher k_R and low D_p/D_r], a larger concentration of the products near the right face helps in building up a larger osmotic pressure, which facilitates the movement from right to left. For such a system if the D_p/D_r is increased beyond a critical, the products with higher diffusivities go away fast from the right face to ensure that the osmotic pressure is higher at the left side leading to a motion from left to right [Fig. 7(b), higher k_R and high D_p/D_r]. The direction of the particle motion has been indicated by the arrows on the plots in which the blue arrow signifies left to right motion, while the red arrow denotes motion from right to left. Concisely, the results discussed in Figs. 4–7 suggest the multiple handles to tune the velocity and direction of the motion of a Janusbot.

Figure 8(a) shows the variations in the particle velocity (u_p) with D_p/D_r. In this case, $\Delta\pi$ ensure that the Janusbot moves toward the left-hand side of the channel, as indicated by $u_p < 0$. In this scenario, as D_p/D_r increases, the particle moves at a higher speed.
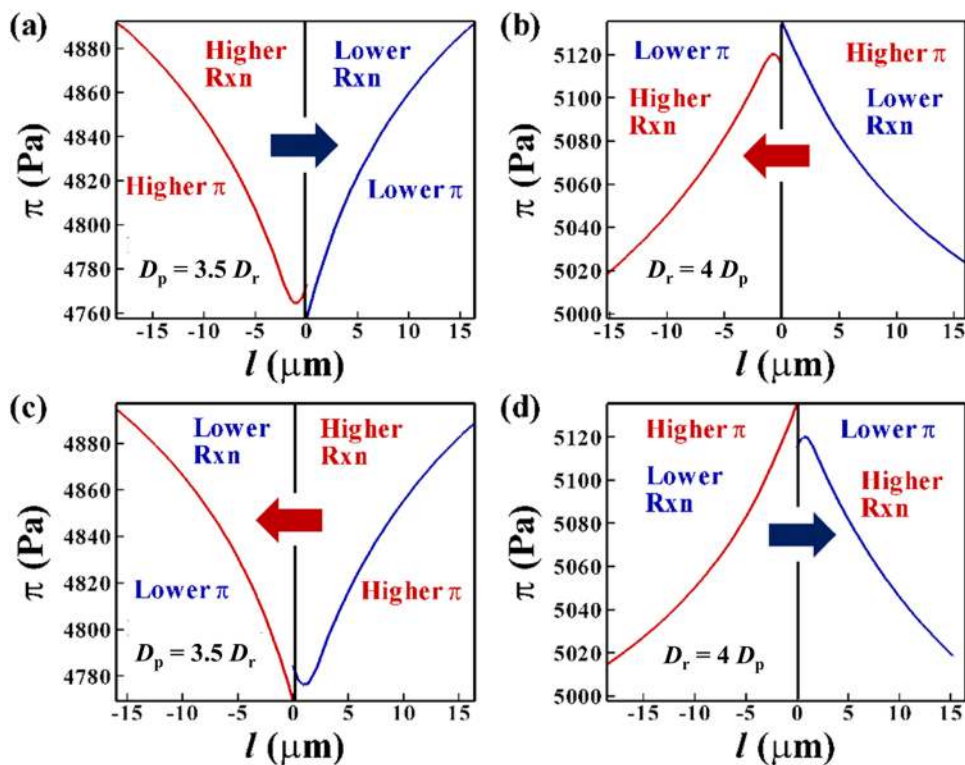
FIG. 7. (a)–(d) Show the near steady state profiles around the particle showing the auto-chemophoretic movement of the space averaged osmotic pressure (π) after 0.4 s. The distance "l" is measured from the surface of the particle. (a) and (c) have higher diffusivity of products (D_p) than the reactants (D_r) with the reaction rates at sides as annotated on the diagrams. (b) and (d) have higher diffusivity of the reactants (D_r) than products (D_p) with the reaction rates as indicated on the diagrams.
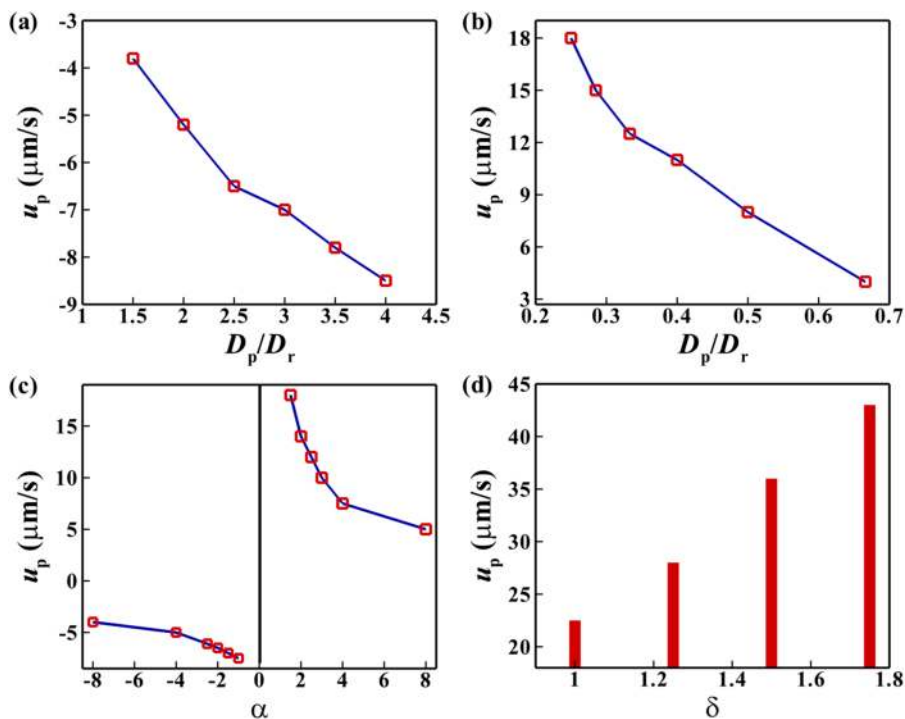

FIG. 8. (a) and (b) Show the variation in the particle velocity (u_p) with the ratio of (D_p/D_r) and (D_r/D_p), respectively, where the right-hand side of the Janusbot has a higher reaction rate (k_R = 8.80 M^{-1} s^{-1}) than the left side (k_L = 0.88 M^{-1} s^{-1}). (c) shows the particle velocity with the variation in the parameter, $\alpha = (k_L - k_R)/[D_r - D_p]$). (d) shows the variation in u_p with the increase in the net stoichiometric coefficient, $\delta = (c + d)/(a + b)$, for the reaction $aA + bB \rightarrow cC + dD$.

Figure 8(b) shows the opposite case, where the reactants have higher diffusivities compared to the products, which enables a larger osmotic pressure buildup to the left of the Janusbot resulting in a motion from left to right. The plot also suggests that in such cases, u_p enhances with the inverse of D_p/D_r, i.e., D_r/D_p. The plots also show that the 5 μm particles achieve a velocity of 5 μm/s–20 μm/s, which is about one to five body length per second under these circumstances. Interestingly, the parameter, $\alpha = (k_L - k_R)/(D_r - D_p)$, can be a useful parameter to fine tune the magnitude and the direction of the Janusbot motions, as shown in Fig. 8(c). For example, $\alpha > 0$ engenders a Janusbot motion toward the right-hand side, whereas $\alpha < 0$ results in a motion toward the left-hand side of the channel. Importantly, the magnitude of the motion increases with the magnitude of α. Importantly, $\alpha = 0$ ensures that the particle becomes stationary.

Other than diffusivity and rate constant of the species, another parameter that significantly influences u_p is $\delta = (c + d)/(a + b)$ for the reaction $aA + bB \rightarrow cC + dD$. Figure 8(d) shows a monotonic increase in u_p until about 10 body lengths/s when δ is increased to 2.5. In brief, Figs. 7 and 8 together summarize the influences of a host of parameters such as rate constants of the reactions at the side of the Janusbots, the diffusivities of the reactants and products, and the stoichiometry of the reactions on the direction and speed of the motion.

From the results, as reported so far, it is well established that auto-chemophoretic migration speeds are very weak (varies from 1 μm/s to 20 μm/s) in nature and lead to only minute drift. This kind of chemophoretic movement can only be expected in a stagnant fluid medium having the components for the reaction. However, in most of the practical situations, external disturbances and other effects may lead to shear flow in the fluid medium, and in most of the natural cases, the magnitude of shear flow exceeds the magnitude of chemophoretic migration. Nevertheless, in those situations, as shown in Fig. 9, the particle floating is guided by the magnitude and direction of the shear flow. A similar shear flow effect on droplet movements in viscous fluid was previously studied by Leal et al.[62] In this part, we have simulated the same auto-chemophoretic migration case with external fluid flow occurring in different directions, such as right to left, left to right, bottom to top, and top to bottom of the channel. It is clearly seen that a weak shear flow (~1 mm/s) subsumed the chemophoretic migration and directed the particle in the direction of shear flow.

B. Guided-chemophoresis

Thus far, we have discussed the results for the auto-chemophoretic Janusbots. However, one of the objectives of this study lies in exploring the chemophoresis of Janus particles in the presence of an external concentration gradient of reactants, as has been found in some of the previous experimental works.[63,64] Figure 10 and Video 2 in the supplementary material show the chemophoretic motion of a Janus particle inside a microfluidic channel of diameter (d) 5 μm and length (l) 15 μm. The supplementary material further describes about Video 2. The external concentration gradient of the reactants has been imposed by enforcing the condition, $c_{ri} = 1$ mol/m^3, at the inlet of the channel and no flux condition to the outlet. Apart from the imposed concentration gradient, a second order catalytic reaction is also considered around the particle wherein the right-hand side of the particle has a higher reaction rate compared to the left-hand side. Furthermore, the product components have a higher diffusivity ($D_p = 4 \times 10^{-9}$ m^2/s) compared to the reactant components ($D_r = 2 \times 10^{-9}$ m^2/s).
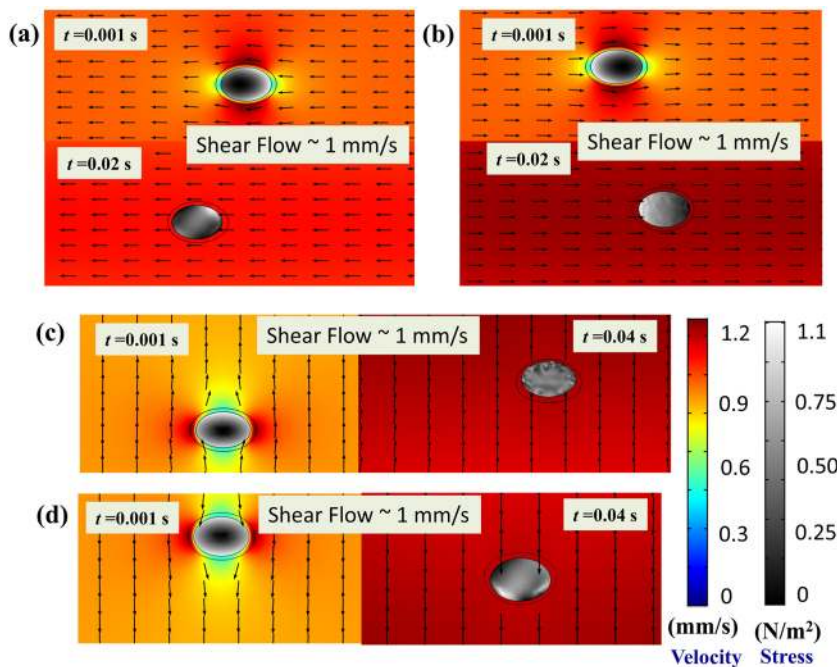

FIG. 9. (a)–(d) Show the directional drift of the particle, which was supposed to self-propel when a shear flow takes place from right to left, left to right, bottom to top, and top to bottom of the channel, respectively.
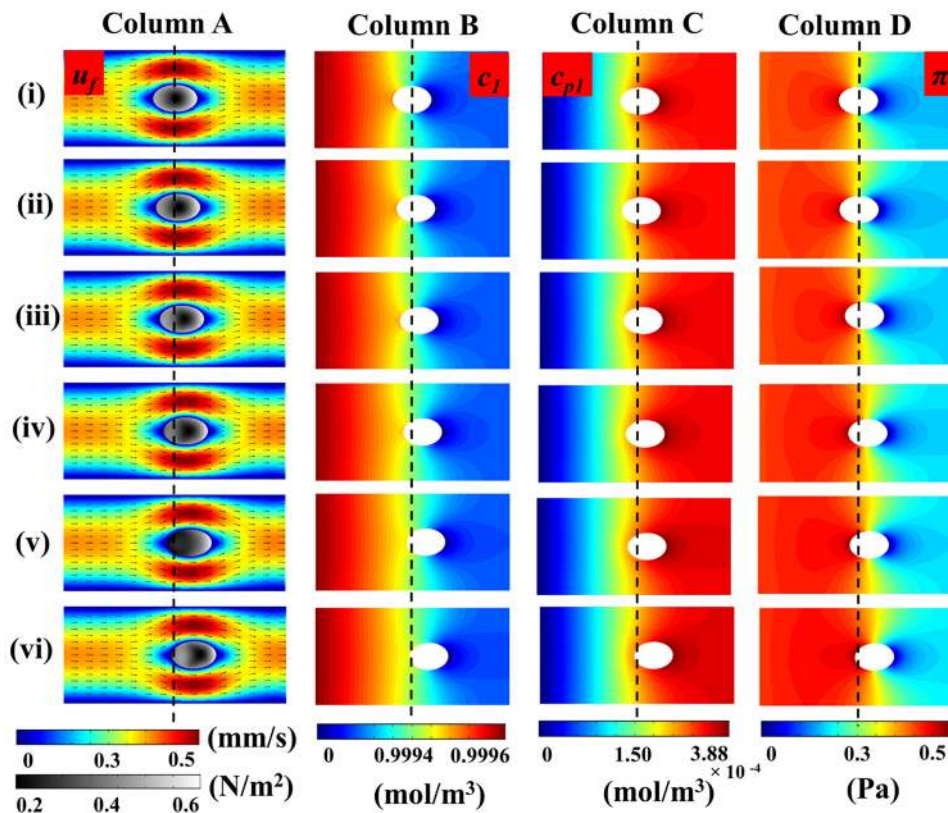
FIG. 10. The chemophoretic motion of a Janus particle moving inside a microfluidic channel of diameter (d_p) 5 μm and length of the channel (l_c) 15 μm. The lengths of the semi-major and semi-minor axes of the elliptical particle are 1 μm and 0.7 μm. (i)–(vi) of column A show the position of the particle inside the channel at time intervals 0 s, 0.4 s, 0.8 s, 1.2 s, 1.6 s, and 2.0 s, respectively. (i)–(vi) of column B show a reactant concentration (c_{r1}) at the respective frames. (i)–(vi) of column C represent the concentration profile of a product (c_{p1}) around the particle at respective time intervals. (i)–(vi) of column D show the osmotic pressure profile around the particle, across the channel.
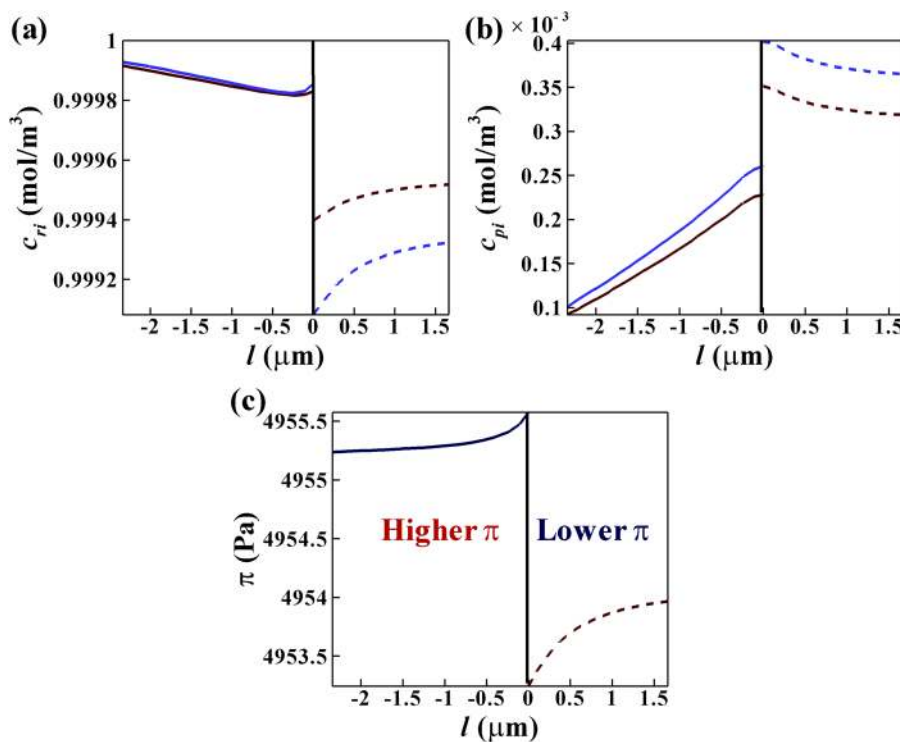

FIG. 11. The concentration profiles (c_{ri} and c_{pi}) along the channel axis. (a) Shows the concentration of the reactants wherein blue lines (lighter shades) represent the concentration of the reactant A, whereas gray lines (darker shades) denotes the concentration of reactant B. (b) Shows the concentration of the products wherein blue lines (lighter shades) represent the concentration of product C and gray lines (darker shade) show the concentration of product D. (c) Shows the osmotic pressure (π) profiles across the particle. Particle surfaces are taken as the starting point and from the particle, while $-l$ and $+l$ represent the distance to the left and right along the axis. Solid lines denote the left-side profiles, and the dotted lines denote the right-side profiles.

It may be noted here that the simulations are performed for 2 s, which is larger than both the reaction and diffusion time scales. Column A shows the positions of the moving particle after 0 s, 0.4 s, 0.8 s, 1.2 s, 1.6 s, and 2.0 s, respectively. Contours of reactant or product concentrations and osmotic pressure are shown in Columns B–D, respectively. Interestingly, in this case, the average speed of the particle has been found to be ~350 nm/s. However, such a speed is much less than the reported one in the previous experiments.[65,66] This is because although the imposed concentration gradient enhances the osmotic pressure gradient across the particle to direct the motion from the left- to right-hand side of the channel, the origin of the sluggish movement lies on the fact that the local osmotic pressure gradient acts in the opposite direction of the motion. Thus, it is imperative that if a concentration gradient is imposed in the opposite direction, it will also facilitate the speed of the Janusbot.

Figure 11 shows the profiles of concentrations of components, and the resulting osmotic pressure around the particle is shown in Fig. 10. The concentrations of A, B and C, D are represented as c_{ri} and c_{pi}, respectively. For the purpose of representation, the coordinate of the particle surface is taken as "0" on both the ends of the particle. The distance from the right-hand side of the particle surface is taken as positive ($+l$), and the distance from the left surface is taken as negative ($-l$). Figure 11(a) shows that the concentrations of the reactants decrease (increase) near (away from) the particle surface due to the reaction, while Fig. 11(b) shows that the products have higher (lower) values near (away from) the particle surface. The reaction and diffusion near the particle surface along with the imposed concentration gradient inside the channel create an imbalance of the osmotic pressure across the particle. Figure 11(c) shows that the local concentration gradient due to the reaction results in the development of a higher (lower) osmotic pressure at the left (right)-hand side of the particle, which eventually helps in the motion of the particle to right of the channel. Briefly, Figs. 10 and 11 together suggest that imposing a reactant concentration gradient can be another way to tune the velocity and direction of the Janusbot propulsion.

VI. CONCLUSIONS

In summary, we propose a comprehensive theoretical framework to explore the finer chemophoretic features of a Janusbot. The motions are governed by the full descriptions of hydrodynamic equations coupled with species balance and fluid–structure interactions. The CFD simulations under a finite element framework uncover that the differential rate kinetics of the reactions on the dissimilar faces of the Janusbot help in building up enough osmotic pressure gradient for a motion as high as 10 body lengths/s. The gradient of osmotic pressure buildup across the Janusbot has been found to be a function of the rate constants of the reactions at the faces of the chemically heterogeneous Janusbot, diffusivities of the species, the stoichiometry of the reaction, and the imposed initial concentration gradient of the reactants. The imbalance of osmotic thrust thus generated is found to be the consequence of the inhomogeneous catalytic reaction at the double-faced Janusbot near the particle surface alongside the net diffusivity of the reactants and products. The numerical simulations uncover that the differential

rate kinetics on the Janusbot faces help in building up an osmotic pressure gradient owing to the variations in the concentrations of the reactants and products, which eventually drives the motor. The presence of an imposed chemical potential gradient across the Janus particle can facilitate as well as reverse the motion of the particle. A composite parameter based on the rate constants at the faces of the Janusbot and diffusivities on the reactants and products, $\alpha = (k_L - k_R)/(D_r - D_p)$, has been identified, which can be employed to tune the speed and the direction of the particle. Furthermore, the stoichiometric ratio $\delta = (c + d)/(a + b)$ for the reaction $aA + bB \rightarrow cC + dD$ is also found to be another useful parameter to accelerate the Janusbot motion. It is also seen that in the presence of surrounding shear flow, the particle moves with an augmented speed in the direction of shear flow and the same indicates the presence of shear flow. Concisely, the study uncovers a number of fundamental aspects of the chemotaxis of a Janusbot, which may be useful for future experiments and applications related to the same.

SUPPLEMENTARY MATERIAL

See the supplementary material for videos 1 and 2 showing auto-chemophoretic and chemophoretic movements, respectively. The detailed description of the videos is given in the doc file.

DATA AVAILABILITY

The data that support the findings of this study are available from the corresponding author upon reasonable request.

REFERENCES

[1] J. A. Perrone, "Model for the computation of self-motion in biological systems," J. Opt. Soc. Am. A **9**, 177 (1992).

[2] M. Yim, W.-M. Shen, B. Salemi, D. Rus, M. Moll, H. Lipson, E. Klavins, and G. Chirikjian, "Modular self-reconfigurable robot systems [grand challenges of robotics]," IEEE Robot. Autom. Mag. **14**, 43 (2007).

[3] M. R. D'Orsogna, Y.-L. Chuang, A. L. Bertozzi, and L. S. Chayes, "Self-propelled particles with soft-core interactions: Patterns, stability, and collapse," Phys. Rev. Lett. **96**, 104302 (2006).

[4] N. Nandi, K. Bhattacharyya, and B. Bagchi, "Dielectric relaxation and solvation dynamics of water in complex chemical and biological systems," Chem. Rev. **100**, 2013 (2000).

[5] A. L. Defranco, J. S. Parkinson, and D. E. Koshland, "Functional homology of chemotaxis genes in *Escherichia coli* and *Salmonella typhimurium*," J. Bacteriol. **139**, 107 (1979).

[6] H. Berg, "Motile behavior of bacteria," Phys. Today **53**(1), 24 (2000).

[7] U. Alon, M. G. Surette, N. Barkai, and S. Leibler, "Robustness in bacterial chemotaxis," Nature **397**, 168 (1999).

[8]H. S. Kruth, "Receptor-independent fluid-phase pinocytosis mechanisms for induction of foam cell formation with native low-density lipoprotein particles," Curr. Opin. Lipidol. **22**, 386 (2011).

[9]S. Burgdorf and C. Kurts, "Endocytosis mechanisms and the cell biology of antigen presentation," Curr. Opin. Immunol. **20**, 89 (2008).

[10]P. Patriarca, P. Dri, K. Kakinuma, and F. Rossi, "Studies on the mechanism of metabolic stimulation in polymorphonuclear leukocytes during phagocytosis. Activators and inhibitors of the granule bound NADPH oxidase," J. Cell. Biochem. **12**, 137 (1976).

[11]F. M. Griffin, J. A. Griffin, J. E. Leider, and S. C. Silverstein, "Studies on the mechanism of phagocytosis. I. Requirements for circumferential attachment of particle-bound ligands to specific receptors on the macrophage plasma membrane," J. Exp. Med. **142**, 1263 (1975).

[12]P. Mitchell, "Chemiosmotic coupling in oxidative and photosynthetic phosphorylation," Biol. Rev. **41**, 445 (1966).

[13]E. A. Kasumov, R. E. Kasumov, and I. V. Kasumova, "A mechano-chemiosmotic model for the coupling of electron and proton transfer to ATP synthesis in energy-transforming membranes: A personal perspective," Photosynth. Res. **123**, 1 (2015).

[14]S. M. Davison and K. V. Sharp, "Transient electrophoretic motion of cylindrical particles in capillaries," Nanoscale Microscale Thermophys. Eng. **11**, 71 (2007).

[15]T. C. Lee and H. J. Keh, "Electrophoretic motion of a charged particle in a charged cavity," Eur. J. Mech., B/Fluids **48**, 183 (2014).

[16]Z. Wu, Y. Gao, and D. Li, "Electrophoretic motion of ideally polarizable particles in a microchannel," Electrophoresis **30**, 773 (2009).

[17]C. Ye, D. Sinton, D. Erickson, and D. Li, "Electrophoretic motion of a circular cylindrical particle in a circular cylindrical microchannel," Langmuir **18**, 9095 (2002).

[18]S. Mitra, S. Mukherjee, A. Ghosh, and D. Bandyopadhyay, "Effects of fluid–structure–interaction and surface heterogeneity on the electrophoresis of microparticles," Ind. Eng. Chem. Res. (published online).

[19]M. Wang, L. He, and Y. Yin, "Magnetic field guided colloidal assembly," Mater. Today **16**, 110 (2013).

[20]W.-T. L. Fan, O. S. Pak, and M. Sandoval, "Ellipsoidal Brownian self-driven particles in a magnetic field," Phys. Rev. E **95**, 032605 (2017).

[21]Y. Yamane, S. Hemmatiyan, J. i. Ieda, S. Maekawa, and J. Sinova, "Spinmotive force due to motion of magnetic bubble arrays driven by magnetic field gradient," Sci. Rep. **4**, 6901 (2014).

[22]K. Yoshikawa, "Spontaneous mode selection of self-motile object under chemical noneqilibricity," Procedia IUTAM **5**, 240 (2012).

[23]J. F. Brady, "Particle motion driven by solute gradients with application to autonomous motion: Continuum and colloidal perspectives," J. Fluid Mech. **667**, 216 (2011).

[24]T. Shigematsu, M. Kurosawa, and K. Asai, Sub-Nanometer Stepping Drive of Surface Acoustic Wave Motor, 2003 Third IEEE Conference on Nanotechnology (IEEE, 2003).

[25]X. Y. Du, M. E. Swanwick, Y. Q. Fu, J. K. Luo, A. J. Flewitt, D. S. Lee, S. Maeng, and W. I. Milne, "Surface acoustic wave induced streaming and pumping in 128° Y-cut LiNbO$_3$ for microfluidic applications," J. Micromech. Microeng. **19**, 035016 (2009).

[26]S. Nedev, S. Carretero-Palacios, P. Kühler, T. Lohmüller, A. S. Urban, L. J. E. Anderson, and J. Feldmann, "An optically controlled microscale elevator using plasmonic Janus particles," ACS Photonics **2**, 491 (2015).

[27]M. Shirsendu, N. Roy, M. Surjendu, and B. Dipankar, "Multimodal chemo-/magneto-/phototaxis of 3G CNT-bots to power fuel cells," Microsyst. Nanoeng. **6**, 19 (2020).

[28]J. B. Keller and M. J. Miksis, "Surface tension driven flows," SIAM J. Appl. Math. **43**, 268 (1983).

[29]N. J. Cira, A. Benusiglio, and M. Prakash, "Dancing droplets: Autonomous surface tension-driven droplet motion," Phys. Fluids **26**, 091113 (2014).

[30]N. J. Suematsu, T. Sasaki, S. Nakata, and H. Kitahata, "Quantitative estimation of the parameters for self-motion driven by difference in surface tension," Langmuir **30**, 8101 (2014).

[31]Y. Yi, L. Sanchez, Y. Gao, and Y. Yu, "Janus particles for biological imaging and sensing," Analyst **141**, 3526 (2016).

[32]S. Granick, S. Jiang, and Q. Chen, "Janus particles," Phys. Today **62**(7), 68 (2009).

[33]D. A. Saville and O. A. Palusinski, "Theory of electrophoretic separations. Part I: Formulation of a mathematical model," AIChE J. **32**, 207 (1986).

[34]C.-H. Lin, J.-H. Wang, and L.-M. Fu, "Improving the separation efficiency of DNA biosamples in capillary electrophoresis microchips using high-voltage pulsed DC electric fields," Microfluid. Nanofluid. **5**, 403 (2008).

[35]B. J. Nelson, I. K. Kaliakatsos, and J. J. Abbott, "Microrobots for minimally invasive medicine," Annu. Rev. Biomed. Eng. **12**, 55 (2010).

[36]J. B. Stock and M. Baker, Chemotaxis (Elsevier, 2009).

[37]J. Adler, "Chemotaxis in bacteria," Science **153**, 708 (1966).

[38]A. G. Vecchiarelli, Y. Seol, K. C. Neuman, and K. Mizuuchi, "A moving ParA gradient on the nucleoid directs subcellular cargo transport via a chemophoresis force," BioArchitecture **4**, 154 (2014).

[39]E. L. Talbot, Drying Inkjet Droplets: Internal Flows and Deposit Structure (Durham University, 2014).

[40]B. Zhang, H. Zhu, M. Zou, X. Liu, H. Yang, M. Zhang, W. Wu, J. Yao, and M. Du, "Design and fabrication of size-controlled Pt-Au bimetallic alloy nanostructure in carbon nanofibers: A bifunctional material for biosensors and the hydrogen evolution reaction," J. Mater. Sci. **52**, 8207 (2017).

[41]A. Brown and W. Poon, "Ionic effects in self-propelled Pt-coated Janus swimmers," Soft Matter **10**, 4016 (2014).

[42]Y. Hong, D. Velegol, N. Chaturvedi, and A. Sen, "Biomimetic behavior of synthetic particles: From microscopic randomness to macroscopic control," Phys. Chem. Chem. Phys. **12**, 1423 (2010).

[43]S. Sengupta, K. K. Dey, H. S. Muddana, T. Tabouillot, M. E. Ibele, P. J. Butler, and A. Sen, "Enzyme molecules as nanomotors," J. Am. Chem. Soc. **135**, 1406 (2013).

[44]J. R. Howse, R. A. Jones, A. J. Ryan, T. Gough, R. Vafabakhsh, and R. Golestanian, "Self-motile colloidal particles: From directed propulsion to random walk," Phys. Rev. Lett. **99**, 048102 (2007).

[45]L. Baraban, S. M. Harazim, S. Sanchez, and O. G. Schmidt, "Chemotactic behavior of catalytic motors in microfluidic channels," Angew. Chem. **125**, 5662 (2013).

[46]K. K. Dey, S. Bhandari, D. Bandyopadhyay, S. Basu, and A. Chattopadhyay, "The pH taxis of an intelligent catalytic microbot," Small **9**, 1916 (2013).

[47]U. M. Córdova-Figueroa and J. F. Brady, "Osmotic propulsion: The osmotic motor," Phys. Rev. Lett. **100**, 158303 (2008).

[48]U. Erdmann, W. Ebeling, L. Schimansky-Geier, and F. Schweitzer, "Brownian particles far from equilibrium," Eur. Phys. J. B **15**, 105 (2000).

[49]T. R. Kline, W. F. Paxton, T. E. Mallouk, and A. Sen, "Catalytic nanomotors: Remote-controlled autonomous movement of striped metallic nanorods," Angew. Chem. **117**, 754 (2005).

[50]P. Calvo-Marzal, K. M. Manesh, D. Kagan, S. Balasubramanian, M. Cardona, G.-U. Flechsig, J. Posner, and J. Wang, "Electrochemically-triggered motion of catalytic nanomotors," Chem. Commun. **2009**, 4509.

[51]J. Wang and J. Qiu, "A review of carbon dots in biological applications," J. Mater. Sci. **51**, 4728 (2016).

[52]I. Lagzi, "Chemical robotics—Chemotactic drug carriers," Cent. Eur. J. Med. **8**, 377 (2013).

[53]J. Parmar, X. Ma, J. Katuri, J. Simmchen, M. M. Stanton, C. Trichet-Paredes, L. Soler, and S. Sanchez, "Nano and micro architectures for self-propelled motors," Sci. Technol. Adv. Mater. **16**, 014802 (2015).

[54]J. Zhuang, B. W. Park, and M. Sitti, "Propulsion and chemotaxis in bacteria-driven microswimmers," Adv. Sci. **4**, 1700109 (2017).

[55]N. Mittal, E. O. Budrene, M. P. Brenner, and A. Van Oudenaarden, "Motility of Escherichia coli cells in clusters formed by chemotactic aggregation," Proc. Natl. Acad. Sci. U. S. A **100**, 013259 (2003).

[56]J. S. King and R. H. Insall, "Chemotaxis: Finding the way forward with Dictyostelium," Trends Cell Biol. **19**, 523 (2009).

[57]J. Taktikos, V. Zaburdaev, and H. Stark, "Modeling a self-propelled autochemotactic walker," Phys. Rev. E **84**, 041924 (2011).

[58]S. Chakraborty, F. Ivancic, M. Solovchuk, and T. Wen-Hann Sheu, "Stability and dynamics of a chemotaxis system with deformed free-surface in a shallow chamber," Phys. Fluids **30**, 071904 (2018).

[59]A. Mozaffari, N. Sharifi-Mood, J. Koplik, and C. Maldarelli, "Self-diffusiophoretic colloidal propulsion near a solid boundary," Phys. Fluids **28**, 053107 (2016).

[60]H. C. W. Chu, S. Garoff, R. D. Tilton, and A. S. Khair, "Advective-diffusive spreading of diffusiophoretic colloids under transient solute gradients," Soft Matter **16**, 238 (2020).

[61]S. K. P. Sanjeevi, J. A. M. Kuipers, and J. T. Padding, "Drag, lift and torque correlations for non-spherical particles from Stokes limit to high Reynolds numbers," Int. J. Multiphase Flow **106**, 325 (2018).

[62]L. G. Leal, "Flow induced coalescence of drops in a viscous fluid," Phys. Fluids **16**, 1833 (2004).

[63]D. Yamamoto and A. Shioi, "Self-propelled nano/micromotors with a chemical reaction: Underlying physics and strategies of motion control," KONA Powder Part. J. **32**, 2 (2015).

[64]H. Stark, "Artificial chemotaxis of self-phoretic active colloids: Collective behavior," Acc. Chem. Res. **51**, 2681 (2018).

[65]A. N. Hoang, C. N. Jones, L. Dimisko, B. Hamza, J. Martel, N. Kojic, and D. Irimia, "Measuring neutrophil speed and directionality during chemotaxis, directly from a droplet of whole blood," Technology **01**, 49 (2013).

[66]C. Beta, T. Fröhlich, H. U. Bödeker, and E. Bodenschatz, "Chemotaxis in microfluidic devices—A study of flow effects," Lab Chip **8**, 1087 (2008).